Vibrational Spectroscopy 87 (2016) 94–98

Contents lists available at ScienceDirect

Vibrational Spectroscopy

journal homepage: www.elsevier.com/locate/vibspec

Step scan T-cell Fourier-transform infrared photoacoustic spectroscopy (FTIR-PAS) for detection of ambient air contaminants

Lixian Liu[a,b], Andreas Mandelis[a,b,*], Huiting Huan[a,b], Kirk Michaelian[b,c], Alexander Melnikov[b]

[a] School of Optoelectronic Information, University of Electronic Science and Technology of China, Chengdu, 610054, China
[b] Center for Advanced Diffusion-Wave and Photoacoustic Technologies (CADIPT), Department of Mechanical and Industrial Engineering, University of Toronto, Toronto, ON, M5S 3G8, Canada
[c] CanmetENERGY, Natural Resources Canada, Devon, AB, T9G 1A8, Canada

ARTICLE INFO

Article history:
Received 15 March 2016
Received in revised form 14 September 2016
Accepted 14 September 2016
Available online 15 September 2016

Keywords:
Air pollutants
FTIR-PAS
Relaxation time
Resonance frequency
Step scan
T-cell

ABSTRACT

The theory of T-cells and their application in Fourier transform infrared photoacoustic spectroscopy (FTIR-PAS) based on a commercial FTIR spectrometer are discussed. This work was undertaken with the view to develop portable compact instrumentation for monitoring air contaminants. A resonant T-cell was determined to be the most appropriate resonator in view of the requirement for the low frequency and the limited space available in the FTIR spectrometer sample compartment. A two dimensional analytical solution with a semi-empirical boundary condition was introduced for resonance frequency prediction. Carbon dioxide (CO_2) gas was the chosen air contaminant. Linear amplitude response to CO_2 concentrations from 1000 to 8000 ppmv was observed, leading to a theoretical detection limit of 4 ppmv. The FTIR-PA phase shift was correlated to varying relaxation times in a mixture of CO_2 and nitrogen (N_2) gases. The analytical solution showed excellent agreement with simulated and experimental data, providing a reliable means for estimating the resonance frequency of the system. The experimental results establish the feasibility of using step-scan T-cell FTIR-PAS for quantitative detection of ambient air pollutants.

1. Introduction

Branched resonators are used in a variety of technologies including vehicles, exhaust systems, air conditioning ducts, and duct regions of turbofan aircraft engines to suppress the low-frequency narrow band noise in pulsating internal flows [1–10]. Since resonance frequency is one of the key elements of resonators, plenty of work has been done for its prediction. Tang and Sirignano [11] assumed one-dimensional wave propagation in both the neck and cavity of such resonator. They discussed three different cases related to ratios of the neck to cavity length and predicted the resonant frequencies. Selamet et al. [9,10] developed an expression for the transmission loss of a side branched resonator with wave motion. Chanaud [12] provided a relationship for the resonance frequency of configurations with a rectangular parallelepiped cavity volume. Polynomial expressions were presented to predict the end correction combined with boundary element modeling results [13]. All of the foregoing methods assumed an infinite length of the main pipe, so that its dimensions have no effect on the resonance frequency of the resonator. In 2005, Wolff et al. introduced a T-cell resonator to the PAS field which is similar to the branched resonator, but with a finite length of the absorption cylinder [14]. In this geometry the diameter of the buffer cylinder cannot be neglected compared to the length of the absorption cylinder and the shear velocity at the buffer input is non-uniform. As a result, there exists no analytical solution describing the PA field for a T-cell [14].

In this paper, a T-cell was integrated as the resonator into a step scan FTIR-PAS based on a commercial FTIR spectrometer. A two-dimensional analytical approach based on circular concentric

---

[*] Corresponding author at: University of Toronto, Center for Advanced Diffusion-Wave and Photoacoustic Technologies (CADIPT),Department of Mechanical and Industrial Engineering, University of Toronto, Toronto, ON, M5S 3G8, Canada/Center for Advanced Diffusion-Wave and Photoacoustic Technologies (CADIPT), Department of Mechanical and Industrial Engineering, University of Toronto, Toronto, ON, M5S 3G8, Canada.
E-mail address: mandelis@mie.utoronto.ca (A. Mandelis).

http://dx.doi.org/10.1016/j.vibspec.2016.09.013
0924-2031/© 2016 Elsevier B.V. All rights reserved.

Helmholtz resonators [9] with a semi-empirical boundary condition was adopted to predict the resonance frequency of the T-cell. This design provides a possible approach for low frequency amplitude modulation compatible with the small-volume sample compartments of modern FTIR spectrometers, in turn creating the possibility of constructing a portable FTIR-PA spectrometer for field applications. To our best knowledge, this is the first time a T-cell is constructed to achieve low-frequency modulation within the compact volume of an FTIR spectrometer compartment. It gives rise to quantitative FTIR-PAS step-scan spectroscopy, and this instrumentation can possibly lead to portable broadband environmental spectroscopic diagnostics and monitoring of several pollutant gases.

2. Photoacoustic theory of T-cells

A T-cell is a unique resonant photoacoustic cell which exhibits low resonance frequency in a limited space. To the best of our knowledge, few approaches have been published for predicting the resonance frequency of T-cells besides finite-element (FEM) analyses. The present study considers a T-cell with absorption, and buffer cylinders compatible with the limited space of an FTIR spectrometer sample compartment, as shown in Fig. 1(a). The objective of this work is to present an analytical solution of T-cell using a semi-empirical boundary condition for calculating the resonance frequency. A simple expression for the resonance frequency is derived, resulting in a fast and efficient approach for determining the length of the resonance cylinder appropriate for the desired frequency. The effective length l_e is defined as the length l_r of the resonator cylinder modified by the end correction δ [15], $l_e = l_r + \delta$. Furthermore l_e is equal to the distance between the top of the resonance cylinder and the first node in the T-section [14] which is obtained through FEM simulation.

A T-cell simulation model was built with Comsol Multiphysics 4.3 software. The geometry of the cell, except for the length of the resonance cylinder, is described in Fig. 1(a). Aluminum walls with two CaF_2 windows were used and a small Proimo EM158* electronic condenser microphone (sensitivity 25.1 mV/Pa at 1 kHz) was sealed with an O-ring on top of the resonance cylinder. A 20-mm-diameter, collimated Gaussian beam (similar to the size of the mid-infrared source in the FTIR spectrometer) was used to simulate the incident optical beam from the FTIR interferometer exciting the T-cell. Lossy boundary conditions were applied due to the thermal and viscous losses at the boundary [16] for calculating the Q factor. A curve-fitting expression of l_e vs. l_r is shown in Eq. (1) according to the FEM simulation results using various lengths of the resonance cylinder:

$$l_e(\mathrm{mm}) = \begin{cases} 0.8691(l_r+2)+12.95, & (l_r < 100\ \mathrm{mm}) \\ 2.567\times10^{-4}(l_r+2)^2+0.8729(l_r+2)+16.28, & (l_r > 100\mathrm{mm}) \end{cases} \tag{1}$$

Fig. 1(b) compares the effective length calculations using Eq. (1) with the FEM results, and the error is within 0.5%.

From Eq. (1) it is seen that

$$\begin{array}{cc} l_e > l_r + l_b & < 90\mathrm{mm} \\ l_r < l_e < l_r + l_b & 90\ \mathrm{mm} < l_r < 100\mathrm{mm} \\ l_e < l_r & l_r > 100\mathrm{mm} \end{array} \tag{2}$$

The set of inequalities (2) is identical to the results in Ref. [14] which concluded that the pressure node was located inside the resonance cylinder when $l_r > 100$ mm, whereas it was outside when $l_r < 100$ mm. Since the main virtue of a T-cell is that it provides a possible approach for low modulation resonance frequencies, the case $l_r < 90$ mm will not be considered further, since the associated resonance frequency is higher than 1 kHz.

For acoustic propagation in the circular and concentric configuration depicted in Fig. 1(a), the harmonic solution of the wave equation $\nabla^2 p = \frac{1}{c^2}\frac{\partial^2 p}{\partial t^2}$, neglecting viscous losses, can be written as $p(r,z,t) = P(r,z)e^{i\omega t}$, yielding a combination of axial and radial modes due to the axial symmetry [8–10]:

$$P_A(r,z) = A_0 e^{-ikz} + \sum_{n=1}^{\infty} A_n J_0\left(\gamma_{j,0n} r\right) e^{ik_{j,0n} z} \tag{3.1}$$

for a wave traveling in the positive z direction, and

$$P_B(r,z) = B_0 e^{ikz} + \sum_{n=1}^{\infty} B_n J_0\left(\gamma_{j,0n} r\right) e^{-ik_{j,0n} z} \tag{3.2}$$

for a wave traveling in the negative z direction. P is the complex amplitude, J_0 is the Bessel function of the first kind and order zero, $k = \omega/c$ is the planar angular wavenumber and $k_{j,on}$ is the wavenumber in the z direction given by $k_{j,0n} = \sqrt{k^2 - \gamma_{j,0n}^2}$; $\gamma_{j,0n} = \alpha_{0n}/r_j$ is the radial wavenumber and r_j refers to the radii (r_b and r_r) of the buffer and resonance cylinders, respectively. α_{0n} is the root of the derivative of the Bessel function $J_0{}'(\alpha_{0n}) = 0$.

The (longitudinal) oscillation velocity of the photoacoustically generated pressure waves is derived from

$$\frac{\partial u}{\partial t} = -\frac{1}{\rho_0}\nabla p$$

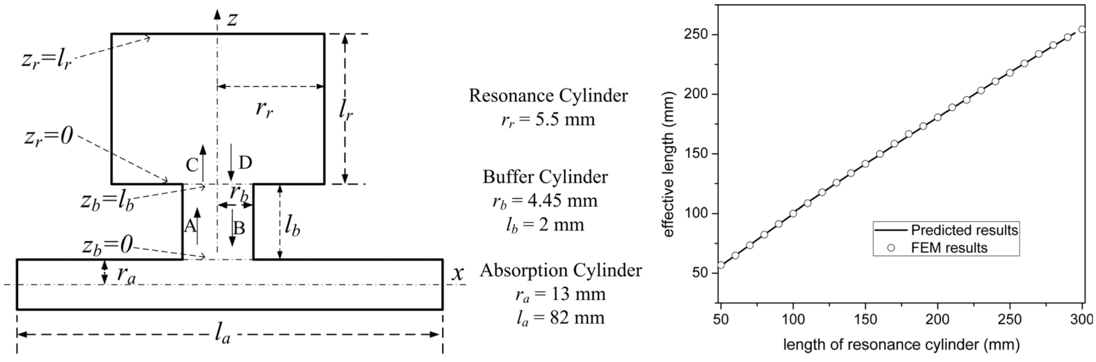

(a) (b)

Fig. 1. (a) The cross-sectional configuration and dimensions of a T-cell. A and B refer to the wave in the buffer cylinder while C and D refer to the wave in the resonance cylinder, respectively; (b) The effective length vs. resonance cylinder length of a T-cell.<!——!>

where u is the displacement, assuming $u(r,z,t)=U(r,z)e^{i\omega t}$. The amplitudes are shown in Eq. (4).

$$U_A(r,z) = \frac{1}{\rho_0 c}A_0 e^{-ikz} - \frac{1}{\rho_0\omega}\sum_{n=1}^{\infty}A_n J_0\left(\gamma_{j,0n}r\right)e^{ik_{j,0n}z} \tag{4.1}$$

$$U_B(r,z) = -\frac{1}{\rho_0 c}B_0 e^{ikz} + \frac{1}{\rho_0\omega}\sum_{n=1}^{\infty}B_n J_0\left(\gamma_{j,0n}r\right)e^{-ik_{j,0n}z} \tag{4.2}$$

Case 1: 90 mm < l_r < 100 mm.

Referring to the length ranges identified in inequalities (2), the first pressure nodes are inside the buffer cylinder when 90mm $< l_r <$ 100mm. Furthermore, there is no significant change of pressure amplitude at these points when the frequency is near resonance. Therefore, the pressure at these points can be assumed to be equal to a constant P_0.

$$(P_A + P_B)|_{z_b = l_b-(l_e-l_r)} = P_0 \tag{5}$$

When both sides of Eq. (5) are multiplied by $J_0\left(\gamma_{b,0s}r\right)r$ $(s: 0,1,2,\ldots\infty)$ and integrated from $r=0$ to $r=r_b$ to take advantage of the orthogonality of the Bessel function set, Eqs. (6) are obtained [17]:For $s=0$

$$A_0 e^{-ik(l_b-(l_e-l_r))} + B_0 e^{ik(l_b-(l_e-l_r))} = P_0 \tag{6.1}$$

For $s = 1,2,3,\ldots\infty$

$$A_s e^{ik_{r,0s}(l_b-(l_e-l_r))} + B_s e^{-ik_{r,0s}(l_b-(l_e-l_r))} = 0 \tag{6.2}$$

The other boundary conditions are shown in Eqs. (7), (9) and (11) [9,10].

At the interface between the buffer and the resonator cylinders $z_b = l_b$, the pressure boundary condition is

$$(P_A + P_B)|_{z_b=l_b} = (P_C + P_D)|_{z_r=0}, for 0 \le r \le r_b \tag{7}$$

Repeating the computational procedure used in the derivation of Eq. (6), one obtains the following expression from Eqs. (3) and (7) for $s = 0$:

$$\begin{aligned}A_0\left(\frac{r_b{}^2}{2}\right)e^{-ikl_b} + B_0\left(\frac{r_b{}^2}{2}\right)e^{ikl_b} &= C_0\left(\frac{r_b{}^2}{2}\right) + \sum_{n=1}^{\infty}C_n\left[\frac{r_b J_1\left(\gamma_{r,0n}r_b\right)}{\gamma_{r,0n}}\right] + D_0\left(\frac{r_b{}^2}{2}\right)\\ &\quad + \sum_{n=1}^{\infty}D_n\left[\frac{r_b J_1\left(\gamma_{r,0n}r_b\right)}{\gamma_{r,0n}}\right]\end{aligned} \tag{8.1}$$

For $s = 1,2,3,\ldots\infty$ the expression becomes:

$$\begin{aligned}A_s e^{ik_{b,0s}l_b}\left[\frac{r_b^2}{2}J_0^2\left(\gamma_{b,0s}r_b\right)\right] + B_s e^{-ik_{b,0s}l_b}\left[\frac{r_b^2}{2}J_0^2\left(\gamma_{b,0s}r_b\right)\right] &= \sum_{n=1}^{\infty}C_n\left[\frac{\gamma_{r,0n}r_b J_1\left(\gamma_{r,0n}r_b\right)J_0\left(\gamma_{b,0s}r_b\right)}{\gamma_{r,0n}^2 - \gamma_{b,0s}^2}\right]\\ &\quad + \sum_{n=1}^{\infty}D_n\left[\frac{\gamma_{r,0n}r_b J_1\left(\gamma_{r,0n}r_b\right)J_0\left(\gamma_{b,0s}r_b\right)}{\gamma_{r,0n}^2 - \gamma_{b,0s}^2}\right]\end{aligned} \tag{8.2}$$

The oscillating pressure-wave velocity boundary conditions at $z_b = l_b$ in the z direction are

$$(u_A + u_B)|_{z_b=l_b} = (u_C + u_D)|_{z_r=0}, for 0 \le r \le r_b \tag{9.1}$$

$$(u_C + u_D)|_{z_r=0} = 0, for r_b \le r \le r_r \tag{9.2}$$

Applying these conditions to Eqs. (4) and (9), yields Eq. (10.1) for $s = 0$,

$$A_0 r_b{}^2 e^{-ikl_b} - B_0 r_b{}^2 e^{ikl_b} = C_0 r_r{}^2 - D_0 r_r{}^2 \tag{10.1}$$

And Eq. (10.2) for $s = 1,2,3,\ldots\infty$:

$$\begin{aligned}&kA_0\left[\frac{r_b J_1\left(\gamma_{r,0s}r_b\right)}{\gamma_{r,0s}}\right]e^{-ikl_b}\\ &\quad - \sum_{n=1}^{\infty}A_n k_{b,0n}\left[\frac{\gamma_{r,0s}r_b J_0\left(\gamma_{b,0n}r_b\right)J_1\left(\gamma_{r,0s}r_b\right)}{\gamma_{r,0s}^2 - \gamma_{b,0n}^2}\right]e^{ik_{b,0n}l_b}\\ &\quad - kB_0\left[\frac{r_b J_1\left(\gamma_{r,0s}r_b\right)}{\gamma_{r,0s}}\right]e^{ikl_b}\\ &\quad + \sum_{n=1}^{\infty}B_n k_{b,0n}\left[\frac{\gamma_{r,0s}r_b J_0\left(\gamma_{b,0n}r_b\right)J_1\left(\gamma_{r,0s}r_b\right)}{\gamma_{r,0s}^2 - \gamma_{b,0n}^2}\right]e^{-ik_{b,0n}l_b}\\ &\quad = -k_{r,0s}C_s\left[\frac{r_r^2}{2}J_0^2\left(\gamma_{r,0s}r_r\right)\right] + k_{r,0s}D_s\left[\frac{r_r^2}{2}J_0^2\left(\gamma_{r,0s}r_r\right)\right]\end{aligned} \tag{10.2}$$

The oscillating pressure-wave velocity in the z direction at the rigid wall on the top of the resonance cylinder ($z_r = l_r$) is taken to be equal to zero:

$$(u_C + u_D)|_{z_r=l_r} = 0 \tag{11}$$

Therefore, Eqs. (4) and (11) give for $s = 0$

$$C_0 e^{-ikl_r} - D_0 e^{ikl_r} = 0 \tag{12.1}$$

And for $s = 1,2,3,\ldots\infty$:

$$C_s e^{ik_{r,0s}l_r} - D_s e^{-ik_{r,0s}l_r} = 0 \tag{12.2}$$

Case 2: l_r > 100 mm.

Considering inequalities (2), the first pressure nodes lie inside the resonance cylinder when l_r > 100 mm. Eq. (13) below is thus considered valid because there is no significant change of pressure amplitude at $z_r = l_r - l_e$ where the amplitude is assumed constant and equal to P_0:

$$(P_C + P_D)|_{z_r=(l_r-l_e)} = P_0 \tag{13}$$

Multiplying both sides of Eq. (13) by $J_0\left(\gamma_{r,0s}r\right)r$ $(s: 0,1,2,\ldots\infty)$ and integrating from $r=0$ to $r=r_r$, the following expression is obtained for $s = 0$

$$C_0 e^{-ik(l_r-l_e)} + D_0 e^{ik(l_r-l_e)} = P_0 \tag{14.1}$$

And for $s = 1,2,3,\ldots\infty$:

$$C_s e^{ik_{r,0s}(l_r-l_e)} + D_s e^{-ik_{r,0s}(l_r-l_e)} = 0 \tag{14.2}$$

Eq. (12) remain valid for this case. C_s and D_s are found to be zero from Eqs. (12.2) and (14.2). It is emphasized that axial propagation is the main oscillation mode because the length to diameter ratio l_r/d_r is quite large, and only one-dimensional propagation in the resonance cylinder is allowed [8,9].

As a result, the pressure at the top of the T-section obtained from Eqs. (3), (12.1) and (14.1) for this case can be simplified:

$$\begin{aligned}P(0,l_r) &\approx C_0 e^{-ikl_r} + D_0 e^{ikl_r}\\ &= 2P_0\left\{\frac{\exp(ikl_r)}{\exp[ik(l_r+l_e)] + \exp[ik(l_r-l_e)]}\right\} = \frac{P_0}{\cos(kl_e)}\end{aligned} \tag{15}$$

There is no significant difference for pressure amplitudes at the nodes when the frequency is near resonance. While the oscillating pressure reaches its maximum on the top of T-section at the resonance frequency and can be evaluated by substituting A_0, A_n, B_0, B_n into Eqs. (3) for *case 1* and calculate from Eq. (15) for *case 2*.

3. Experiments and results

The step scan FTIR-PAS set up was based on a commercial FTIR spectrometer (Bruker Vertex 70), with an integrated T-cell for photoacoustic signal detection and gas dilution assembly for mixing CO_2 and N_2 gases. The incident beam from the interferometer was modulated with a chopper and directed inside the resonator. CO_2 was chosen as the gas to be analyzed. Several concentrations were prepared using a home-made apparatus, utilizing flow meters to set the rate of each tube to the desired value. The details of the system configuration are described in Ref. [16].

Fig. 2(a) compares the variation of resonance frequency vs. length of the resonance cylinder between the two-dimensional analytical solutions, Eqs. (3), (6), (8), (10) and (12) for *case 1* and Eq. (15) for *case 2*, with the FEM approach. There is excellent agreement between the two approaches with the analytical solution accurately predicting the resonance frequency. Fig. 2(b) shows the amplitude response of the T-cell designed for the gas detection experiment with the length of the resonance cylinder equal to 300 mm. The analytical and simulated resonance frequencies (342 Hz) are both consistent with experimental results. However, the full width half maximum (FWHM) of the amplitude peak of the analytical solution is narrower because viscous and thermal losses were neglected. The *Q* factor [18] was determined to be 55.5 from the experimental results. The incident light power at ca. 4.3 μm (the absorption peak of CO_2) was estimated to be 12.6 μW according to the globar (MIR source in the FTIR spectrometer) manufacturer's information. Thus the cell constant *C* for the FTIR-PAS system was calculated to be approximately 2063 Pa cm/W based on Eq. (16) [19] where α is the absorption coefficient, and *W* is the incident light power.

$$C = P(0, l_r)/(\alpha W) \tag{16}$$

While the accuracy of the FWHM amplitude peak is better with FEM, the simulation method is time consuming. Moreover, its accuracy depends sensitively on the mesh quality. A finer mesh implies a larger number of elements, hence longer computation time and larger computer memory are needed. Therefore, it is more efficient to calculate the resonance frequency and the associated resonance cylinder (T-cell) length using the analytical solution and then fine-tune parameters with FEM simulations for the cell dimensions desired and *Q* factor, rather than simulating a large number of resonance cylinder lengths using FEM to determine the required frequency and dimensions.

Fig. 3 depicts the concentration dependence of the amplitude and phase signals at the CO_2 absorption peak ($2349\ cm^{-1}$) between 8000 and 1000 ppmv in the step scan FTIR-PAS experiments. It is observed that the measured amplitude displays a linear dependence on concentration, an important result that obviates the need for complicated non-linear calibration in practice [20]. The signal value at the absorption peak for 5000 ppmv is 0.143 (arbitrary unit), and the standard deviation between the best-fit straight line and the measured data in the range of $3200–3250\ cm^{-1}$ (the range is far away from the absorption peak) is 9.435×10^{-5}. This value can be taken to be the baseline noise level using the method described in Ref. [21]. Thus, the signal to noise ratio (SNR) is 1515.5 ($0.143/9.435 \times 10^{-5}$), and the detection limit is 4 ppmv (5000 ppmv/1515.5) for SNR = 1. These results are comparable with the 4 ppm detection limit in Ref. [21] which, however, used a system working at 470 mbar with an optical cantilever-based detector. The step scan FTIR-PAS system presented here is simpler and more convenient because it works at ambient conditions and employs a condenser microphone as the detector.

The relationship between PA phase signal φ and CO_2 concentration can be expressed as [22]

$$\tan(\varphi - \varphi_0) = \omega\tau/C \tag{17}$$

where τ is the relaxation time of the gas mixture at 1 atm, $\omega = 2\pi f$ is the angular modulation frequency, *C* is the CO_2 concentration and φ_0 is the reference offset which is determined by the experimental setup (φ_0 is 4° in the FTIR-PAS system). The relaxation time at ambient (normal) pressure and temperature (NPT) is approximately $\tau_{CO_2} = 7.5\ \mu s$ for pure CO_2 [22]. Eq. (17) neglects the relaxation time of N_2 because its vibrational relaxation time, approximately 4 ± 2s at NPT [23], is too long to contribute to the phase profile of Fig. 3(b). Therefore, the theoretical PA phase signal increases as the CO_2 concentration in the mixture decreases, a trend similar to the experimental phase data in Fig. 3(b). The deviation in Fig. 3(b) may occur because the absorption coefficient for pure CO_2 is on the order of $10^2\ cm^{-1}$ at NPT in the 4.3 μm region [24]; this means that the sample can no longer be considered as optically thin (the length of the absorption cylinder is 82 mm). In other words, the dimension and shape of the photoacoustic source induced by the absorption of the incident 4.3 μm radiation

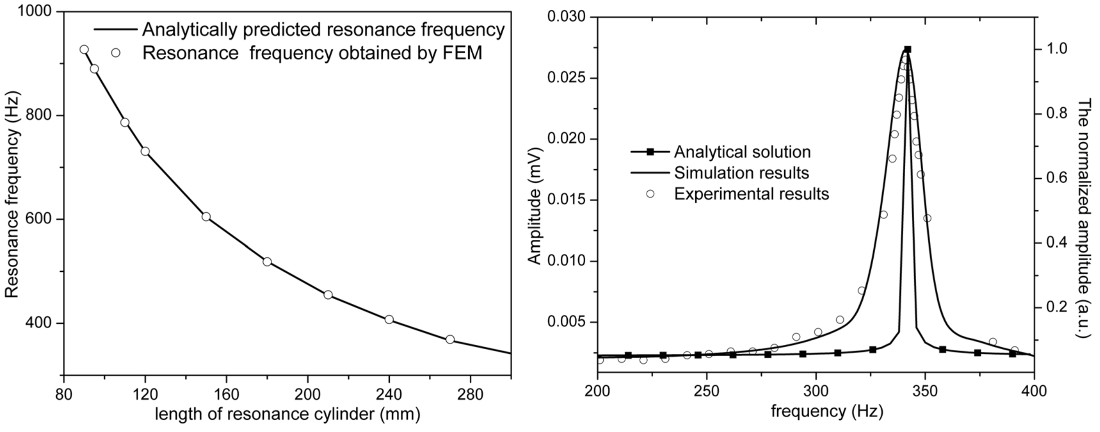

(a) (b)

Fig. 2. (a) Resonance frequency of the T-cell as a function of resonance cylinder length; (b) Amplitude response of the T-cell.

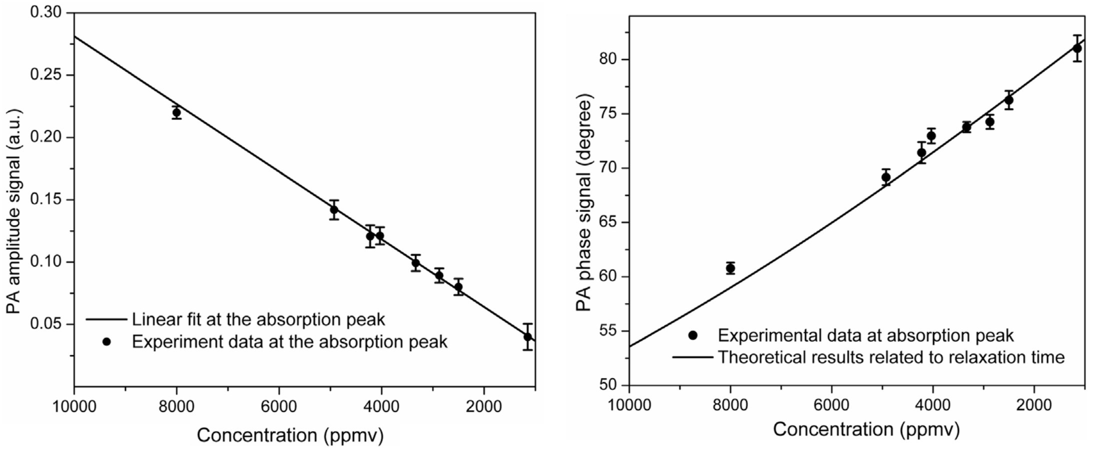

(a) (b)

Fig. 3. (a) step scan FTIR-PAS amplitude and (b) phase signal of CO_2 at the 2349 cm^{-1} absorption peak.

changes with CO_2 concentration, likely causing a change in the phase signal. Another possible cause for the deviation is an error in the gas dilution with the home-made apparatus, which could produce some inaccuracy in CO_2 concentration. The phase signal is unlikely to be directly related to trace gas CO_2 concentration by means of nonradiative relaxation, since relaxation times among different ambient gases at NPT are not significantly different and are short compared to the step-scan chopping rate [25]. Nevertheless, the phase shift presented here is related to the overall vibrational relaxation time with indirect dependence on the impurity gas concentration and, along with the amplitude, establishes the validity of the analytical and FEM computational approaches reported herein, as well as the sensitivity of the step scan T-cell FTIR-PAS system to CO_2 mixtures with N_2.

4. Conclusions

A step scan FTIR-PAS system based on a commercial FTIR interferometer and a T-cell as the resonator was assembled and tested in this work. A two-dimensional analytical solution with a semi-empirical boundary condition was developed and found to yield accurate resonance frequency predictions. The analytical and simulated FEM resonance frequencies exhibited excellent agreement with the experimental data. However, the FWHM of the analytical solution was narrower than the FEM-simulated width and the measured frequency response profile because viscous and thermal losses were neglected. The theoretical detection limit was calculated to be 4 ppmv. The agreement of the phase shift with theoretical results corrected to relaxation time demonstrates the validity of the theoretical and instrumental step scan T-cell FTIR-PAS system approach. In mixtures of CO_2 with N_2, the amplitude signal was found to be linear with CO_2 concentration ranging from 8000–1000 ppmv, which proved the capability of step-scan T-cell FTIR-PAS as a quantitative analysis technique for trace gas detection in air.

Acknowledgments

A.M. is grateful to the Canada Research Chairs and to the Natural Sciences and Engineering Research Council of Canada (NSERC) for a Discovery Grant. A.M. also gratefully acknowledges the Chinese Recruitment Program of Global Experts (Thousand Talents). L.-L is grateful to the China Scholarship Council (CSC) for an international student grant. Valuable advice by Dr. Christoph Haish on the PA FEM analysis is also gratefully acknowledged.

References

[1] M.L. Munjal, Acoustics of Ducts and Muffler, Wiley-Interscience, New York, 1987.
[2] V. Dubos, J. Kergomard, A. Khettabi, J.-P. Dalmont, Acustica 85 (1999) 153–169.
[3] A.D. Lapin, Sov. Phys.-Acoust. 7 (1961) 171–175.
[4] C.J. Nederveen, D.W. van Wulfften Palthe, Acustica 13 (1963) 65–70.
[5] W. Soedel, E. Padilla Navas, B.D. Kotalik, J. Sound Vib. 30 (1973) 263–277, doi: http://dx.doi.org/10.1016/S0022-460X(73)80238-X.
[6] A. Selamet, N.S. Dicky, J.M. Novak, J. Sound Vib. 187 (1995) 358–367, doi:http://dx.doi.org/10.1006/jsvi.1995.0529.
[7] A. Selamet, P.M. Radavich, SAE 95 (1995) 1263–1275, doi:http://dx.doi.org/10.4271/951263.
[8] A. Selamet, N.S. Dickey, P.M. Radavich, J.M. Novak, SAE 94 (1994) 0612–0623, doi:http://dx.doi.org/10.4271/940612.
[9] A. Selamet, J. Acoust. Soc. Am. 101 (1997) 41–51, doi:http://dx.doi.org/10.1121/1.417986.
[10] A. Selamet, Z.L. Ji, J. Acoust. Soc. Am. 107 (2000) 2360–2369, doi:http://dx.doi.org/10.1121/1.428622.
[11] P.K. Tang, W.A. Sirignano, J. Sound Vib. 26 (1973) 247–262, doi:http://dx.doi.org/10.1016/S0022-460X(73)80234-2.
[12] R.C. Chanaud, J. Sound Vib. 178 (1994) 337–348, doi:http://dx.doi.org/10.1006/jsvi.1994.1490.
[13] Z.L. Ji, J. Sound Vib. 283 (2005) 1180–1186, doi:http://dx.doi.org/10.1016/j.jsv.2004.06.044.
[14] M. Wolff, H.G. Groninga, B. Baumann, B. Kost, H. Harde, Acta Acust. 91 (2005) 99.
[15] T.D. Rossing, Handbook of Acoustics, Springer Dordrecht Heidelberg, London New York, 2014.
[16] L. Liu, A. Mandelis, A. Melnikov, K. Michelian, H. Huan, Int. J. Thermophys. 37 (2016) 64, doi:http://dx.doi.org/10.1007/s10765-016-2070-0.
[17] J. Miles, J. Acoust. Soc. Am. 20 (1944) 652–664, doi:http://dx.doi.org/10.1121/1.1916257.
[18] A. Miklós, P. Hess, Rev. Sci. Instrum. 72 (2001) 1937–1955, doi:http://dx.doi.org/10.1063/1.1353198.
[19] F.G.C. Bijnen, J. Reuss, F.J.M. Harren, Rev. Sci. Instrum. 67 (1996) 2914–2923, doi:http://dx.doi.org/10.1063/1.1147072.
[20] J. Uotila, V. Koskinen, J. Kauppinen, Vib. Spectrosc. 38 (2005) 3–9, doi:http://dx.doi.org/10.1016/j.vibspec.2005.02.002.
[21] C.B. Hirschmann, J. Uotila, S. Ojala, J. Tenhunen, R.L. Keiski, Appl. Spectrosc. 64 (2010) 293–297, doi:http://dx.doi.org/10.1366/000370210790918490.
[22] I.M. Macfarlane, H. Young, Trans. Faraday Soc. 62 (1966) 2655–2666, doi: http://dx.doi.org/10.1039/TF9676302093.
[23] R.F. Barrow, D.A. Long, J. Sheridan, Molecular Spectroscopy, vol. 4, Chemical Society, London, 1976.
[24] L.S. Rothman, D. Jacquemart, A. Barbe, D. Chris Benner, M. Birk, L.R. Brown, M.R. Carleer, C. Chackerian Jr., K. Chance, L.H. Coudert, V. Dana, V.M. Devi, J.-M. Flaud, R.R. Gamache, A. Goldman, J.-M. Hartmann, K.W. Jucks, A.G. Maki, J.-Y. Mandin, S.T. Massie, J. Orphal, A. Perrin, C.P. Rinsland, M.A.H. Smith, J. Tennyson, R.N. Tolchenov, R.A. Toth, J. Vander Auwera, P. Varanasi, G. Wagner, J. Quant. Spectrosc. Radiat. Transf. 96 (2005) 139–204, doi:http://dx.doi.org/10.1016/j.jqsrt.2004.10.008.
[25] V.P. Zharov, V.S. Letokhov, Laser Optoacoustic Spectroscopy, Springer-Verlag, Berlin, 1986.